

We are IntechOpen, the world's leading publisher of Open Access books Built by scientists, for scientists

6,900

Open access books available

186,000

International authors and editors

200M

Downloads

Our authors are among the

154

Countries delivered to

TOP 1%

most cited scientists

12.2%

Contributors from top 500 universities



WEB OF SCIENCE™

Selection of our books indexed in the Book Citation Index
in Web of Science™ Core Collection (BKCI)

Interested in publishing with us?
Contact book.department@intechopen.com

Numbers displayed above are based on latest data collected.
For more information visit www.intechopen.com



Diagnostics of a Crater Growth and Plasma Jet Evolution on Laser Pulse Materials Processing

A. Yu. Ivanov and S. V. Vasiliev

Additional information is available at the end of the chapter

<http://dx.doi.org/10.5772/48703>

1. Introduction

The scheme of the experimental setup used in the study is presented in Fig. 1. The radiation of the GOR-100M ruby laser (1) ($\lambda = 0.694 \mu\text{m}$) operating in the free oscillation regime (pulse duration $\tau \sim 1.2 \text{ ms}$, Fig. 2) or rhodamine laser ($\lambda = 0.58 \mu\text{m}$), pulse duration $\tau \sim 20 \mu\text{s}$) passed through the focusing system (2) and was directed through the hole in the electrode (3) onto the sample (4) that served as the second electrode and was mounted in air at a pressure of 10^5 Pa . The radiation spot diameter with sharp edges on the sample was varied in the course of the experiments from 1 to 2 mm.

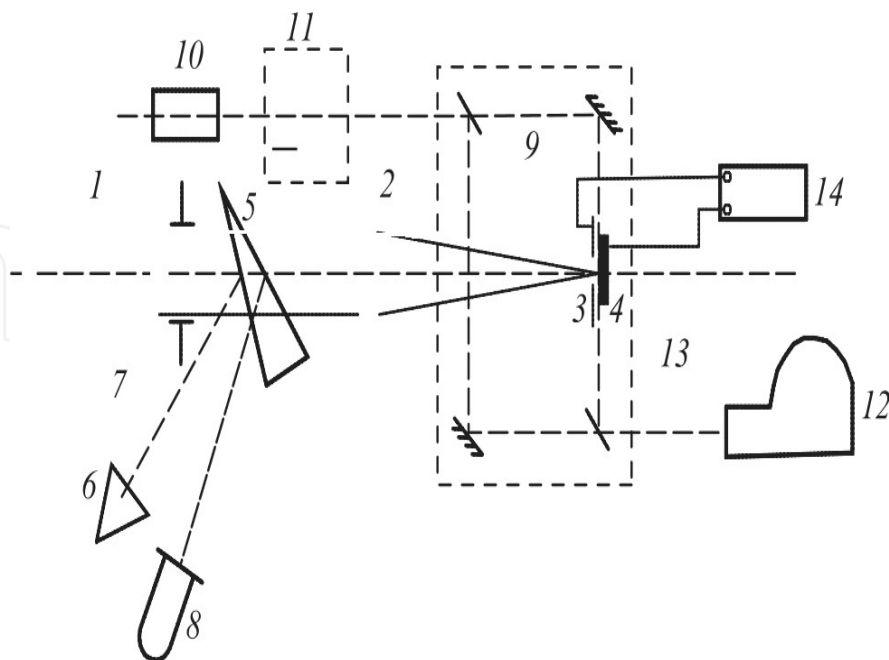


Figure 1. The experimental setup schematic diagram.

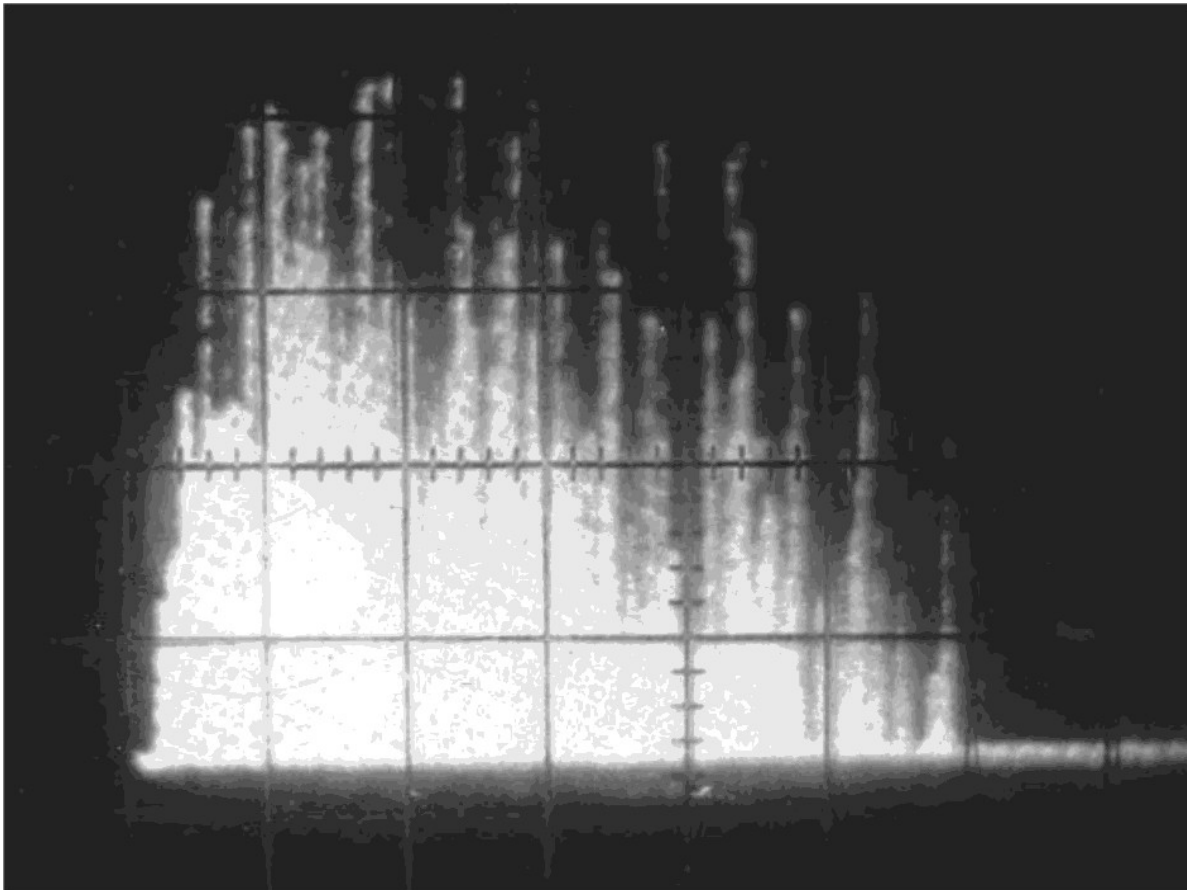


Figure 2. Oscillogram of the radiation pulse from the GOR-100M laser. The scanning rate is 200 $\mu\text{s}/\text{div}$.

From the front face of the glass wedge (5) a part (4%) of laser radiation was directed into the IMO-2N energy meter (6), whose entrance window was located in the focal plane of the lens (7). The energy of the laser pulses varied from 5 to 60 J. The FEK-14 coaxial photodetector (8), the signal from which was coupled to the S8-13 oscilloscope, was used to record the temporal shape of the laser pulse. The voltage was applied to the electrodes (3, 4) from the source (14), built on the basis of the UN 9/27-13 voltage multiplier of the TVS-110 unit. The source allowed the voltage variation within 25 kV and its stabilization in the course of the experiment.

To study the spatial and temporal evolution of the laser plasma plume in the course of laser radiation action on the sample, we used the method of high-speed holographic motion-picture recording. The interelectrode gap was placed in one of the arms of a Mach-Zehnder interferometer (9), which was illuminated with the radiation of the ruby laser (10) ($\lambda = 0.694 \mu\text{m}$) operating in the free oscillation regime. The pulse duration of the radiation amounted to $\sim 400 \mu\text{s}$. The transverse mode selection in the probing laser was accomplished using the aperture, placed in the cavity, and the longitudinal mode selection was provided by the Fabry-Perot cavity standard used as the output mirror. The probing radiation after the collimator (11) was a parallel light beam with the diameter up to 3 cm, which allowed observation of the steam-plasma cloud development.

The interferometer was attached to the SFR-1 M high-speed recording camera (12), in which the plane of the film was conjugate with the meridian section of the laser beam, acting on the sample, by means of the objective (13). The high-speed camera operated in the time magnifier regime. The described setup allowed recording of time-resolved holograms of the focused image of the laser plasma plume. Separate holographic frames provided temporal resolution no worse than $0.8 \mu s$ (the single frame exposure time) and the spatial resolution in the object field $\sim 50 \mu m$. The error in the determination of the electron density was $\sim 10\%$ and it was governed by the precision with which the shifts of the fringes could be determined in the photographically developed interference patterns.

The diffraction efficiency of the holograms allowed one to reconstruct and record interference and shadow pictures of the studied process under the stationary conditions. The shadow method was most sensitive to $\text{grad } n$, so that the nature of the motion of the front of a shock wave outside the laser plasma and of the motion of the plasma jet could be determined from the reconstructed shadow patterns. This gave information on the motion of the shock front and the laser plasma front generated at the surfaces of metal samples. It was found that the nature of the motion of the shock wave front was practically independent of the target material and was governed primarily by the average power density of the laser radiation.

The reconstructed interference patterns were used to determine the spatial and temporal distributions of the electron density in a laser plasma plume.

The reliability of the results obtained by the method of fast holographic cinematography was checked by determination of the velocity of the front of a luminous plasma jet by a traditional method using slit scans recorded with a second SFR- 1M streak camera.

To study the surface shape of the crater that appears on the plate, we used the fringe projection method, which in the present case appeared to be more efficient than holographic methods of surface relief imaging and the stereophotogrammetric method, since, already at the stage of fringe projecting, it allowed obtaining a picture with controllable sensitivity of measurements and sufficiently good visibility of fringes, controlled visually. The sensitivity of measurements (relative fringe displacement) was set by changing the period of the projected fringes, and the good visibility was provided by changing the angle of illumination of the studied surface till removing the light flares from the crater surface. The present method is thoroughly described and successfully used in [2].

The optical scheme of the apparatus used to visualize the topography of crater is shown on Figure 2. Radiation of helium-neon laser 1 LGN-215 collimated by telescopic system 2 was used to illuminate Mach-Zehnder interferometer 3. The interference picture was then projected to the sample 4 being studied. During the above procedure a system of dark and light strips was observed on the treated surface, and besides the configuration of strips was connected synonymously with the depth of the crater in the point of interference

$$h = d \cdot \Delta k / (tg\beta + tg\gamma).$$

Here d is a period of interference strips on the flat (nonirradiated) zone of the target, Δk - the displacement of a dark strip, β - an angle between the perpendicular to the surface of the irradiated sample and the projected interference surface, γ - an angle between the normal to the surface of the irradiated sample and the optical axis of the photographic camera.

The sample surface was optically mated with the picture surface 5 with the help of the objective "Helios-44-2". Contour stripes on the picture surface were fixed on the photographic film.

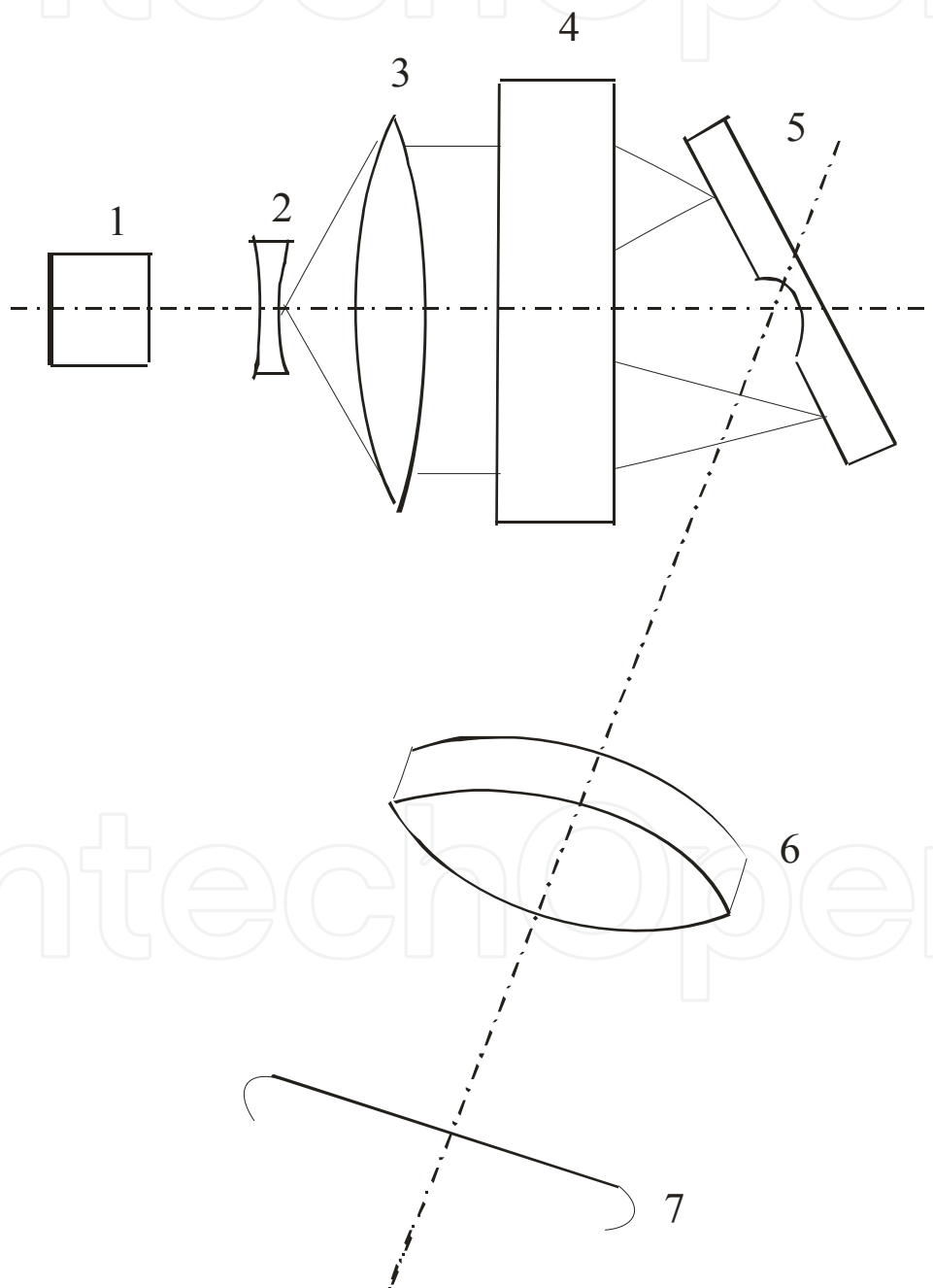


Figure 3. Schematic diagram of the visualization apparatus.

2. Experimental results and discussion

The experimental results have shown that at any polarity of the applied voltage [with positive or negative potential at the irradiated sample with respect to the electrode (3) the topography of the crater is practically identical and is determined by the energy distribution over the focusing spot of the laser radiation (Figs 4, 5).

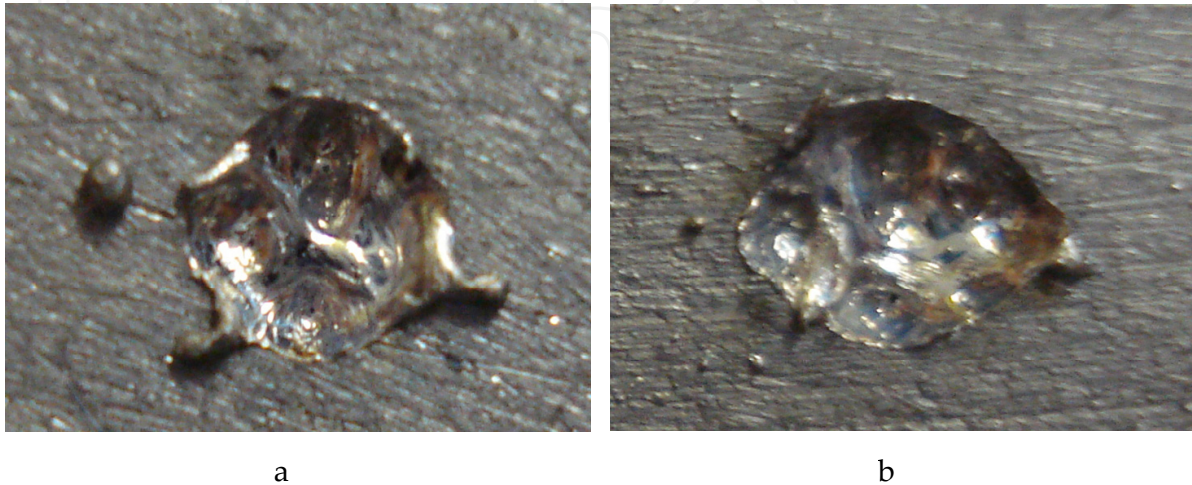


Figure 4. Photographs of the craters obtained under the action of laser pulses on the target in the absence of the external electric field (a) and in the presence of the field (b).

Figures 6 a - c display the interferograms, reconstructed from the holograms recorded at different instants in the course of high-speed holographic motion-picture shooting. The figure clearly illustrates both the initial stage of the laser torch development and the plasma flow around the electrode (3) at different directions of the external electric field strength vector.

Figures 6 d - f represent the data on the distribution of concentration of free electrons in the plasma of an evaporated metal at different instants, obtained by processing the interferograms [1]. Although the energy distribution over the laser radiation focusing spot is not uniform, the lines of equal concentration are practically smooth, which is an evidence of relatively uniform ionization of the eroded substance steams. It is essential that, despite a substantial increase in the plasma formation over time, the mean electron concentration in the torch remains practically unchanged and even slightly grows, which may be associated both with a constant increase in the mass of emitted substance and with secondary ionization of the plasma by the laser radiation. Note, that the presence of an external electric field weakly affects the concentration of electrons in the laser plasma plume.

When the interelectrode separation was 2 cm, the maximal transverse size of the steam-plasma cloud at the surface of the electrode (3) for negative voltage on the target was 2 cm and in the absence of the external electric field it was 1.5 cm. This may be observed both in the interferograms and by the burn on the polyethylene film protecting the second electrode. As seen from interferograms, after reaching the second electrode in 56, 64, and 72 μs ,

respectively, the steam-plasma cloud practically does not grow in the transverse dimensions. Probably it is due to the flowing out of the plasma from the interelectrode gap through the hole in the electrode (3), which is used for passing the laser radiation to the target (the hole diameter being 1 cm).

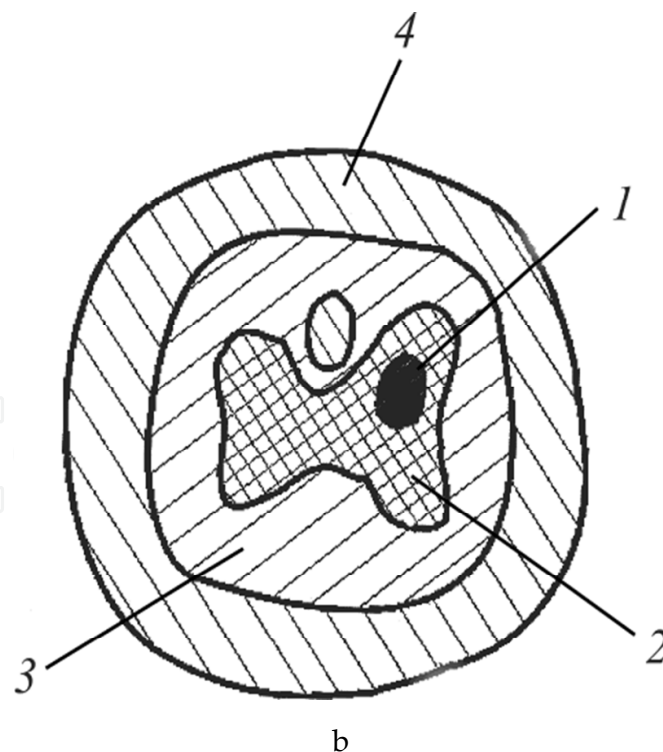
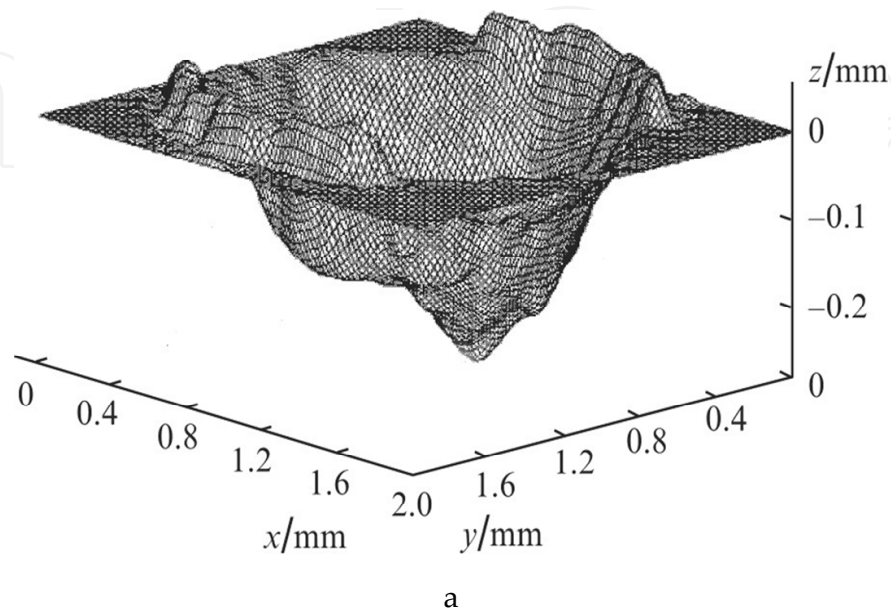


Figure 5. Volume topogram of a crater (a) and the distribution of light energy density over the transverse cross-section of the laser beam (b): 4.5 (1), 3.5 (2), 1.2 (3), and 0.8 J mm⁻² (4).

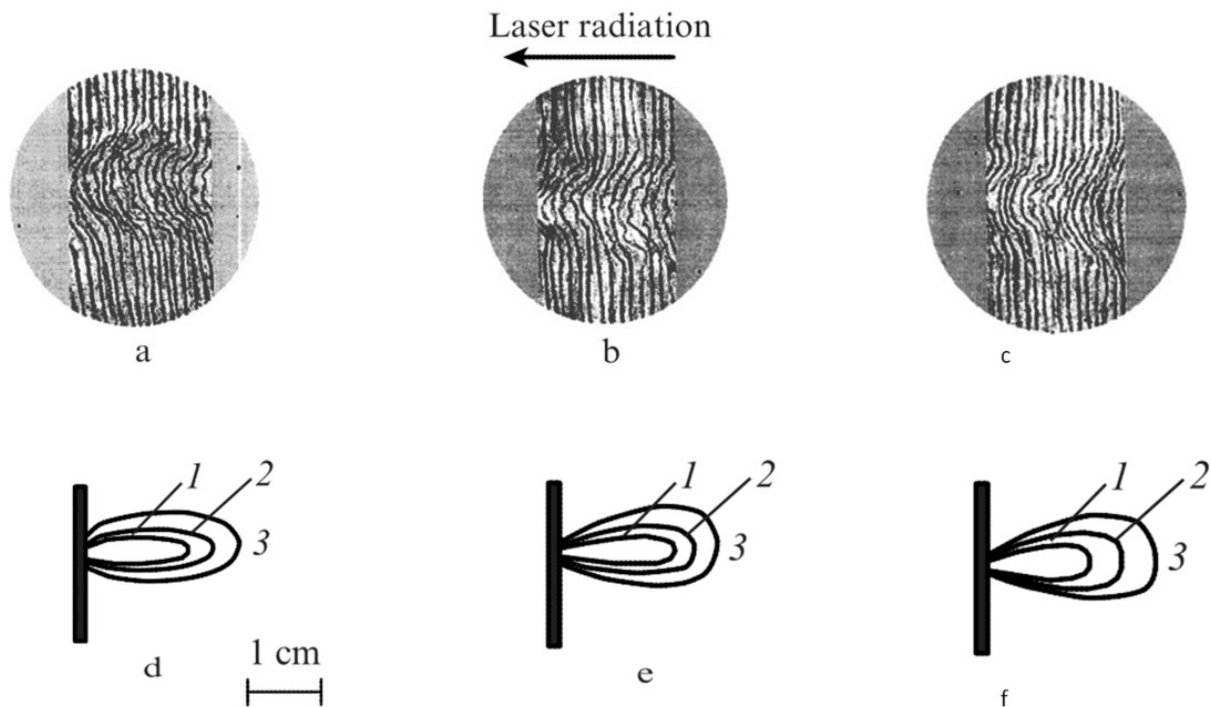


Figure 6. Interferograms of laser plasma torches (a, b, c) and electron concentration isolines in them (d, e, f) at the negative target potential (b, e) and at the positive target potential (c, f) at the instants $72 \mu\text{s}$ after the onset of the laser action; curve (1) corresponds to the electron concentration 5×10^{18} , curve (2) to 2.5×10^{18} , and curve (3) to 10^{18} cm^{-3} .

Figure 7 presents the time dependences of the plasma torch front motion velocity at different directions of the external electric field strength vector, calculated by using the information, obtained by analyzing the temporal variation of the interferograms. It is seen that even when the plasma front reaches the electrode (3), its velocity not only does not decrease (which is typical for late stages of the laser plasma torch existence [3]), but even increases; this happens both in the presence of the external electric field of any orientation and in the absence of the field. As already mentioned, this is due to the permanent and significant increase in the mass of the material, carried out under the action of laser radiation on the irradiated sample, as well as to the secondary ionization of plasma by laser radiation.

The maximal expansion velocity of the plasma torch amounted to 350 m/s for the negative voltage at the target, 310 m/s in the absence of the external electric field, and 270 m/s for the positive voltage applied to the target.

Our investigation showed that the time evolution of the leading edge of a luminous plasma moving away from the surface of a sample, deduced from the slit scans, differed from the time evolution of the front of the plasma jet, which was recorded by the shadow method. This allowed us to conclude that the concentration of the heavy particles, responsible for the radiation emitted by the plasma, was low at the front of the laser plasma jet, whereas the electron density was sufficient for reliable determination of the contribution of electrons to refraction in a hologram.

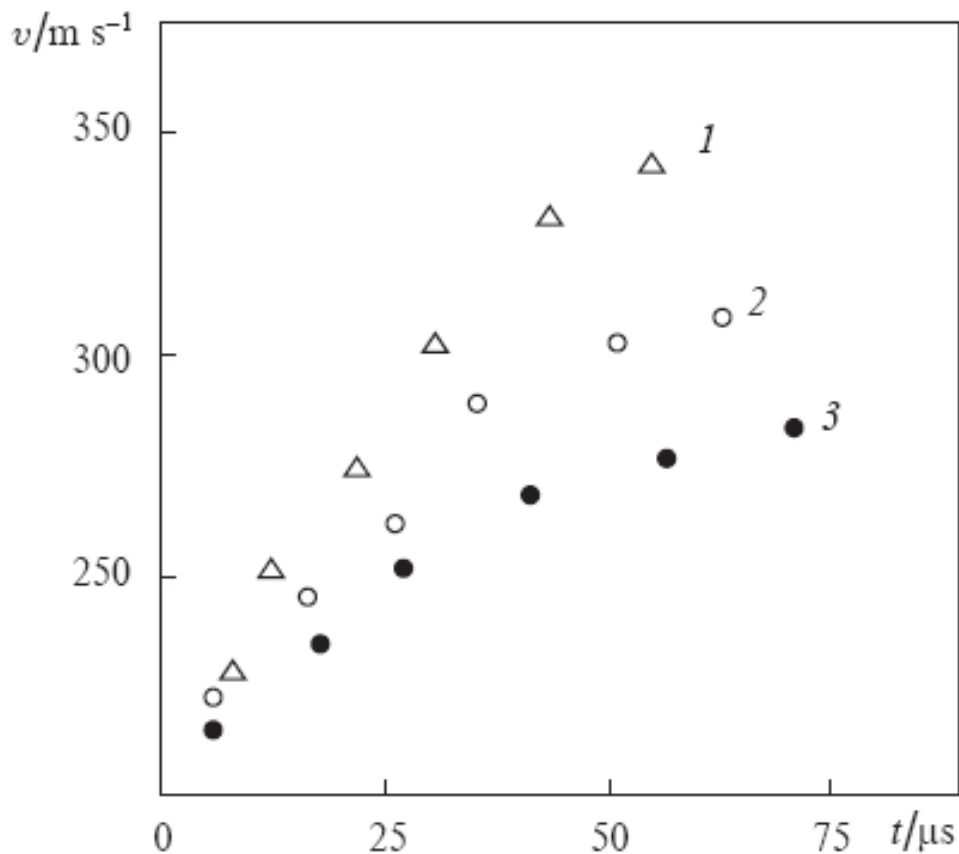


Figure 7. Time dependences of the velocity of the plasma torch front motion at the negative target potential (1), in the absence of the field (2), and at the positive target potential (3).

The distribution of the density of cold air was determined and the electron density distribution was refined by two-wavelength holographic cinematography. We supplemented the system shown schematically in Fig. 1 with a second probe laser and an SFR-1M camera which recorded holograms at the wavelength of the radiation emitted by this laser. The second source of probe radiation was a laser utilizing a rhodamine 6G solution excited by a coaxial flashlamp. The use of a standard power supply system from a GOR-100M laser made it possible to generate output radiation pulses of 30 – 40 μs duration. The line width was reduced employing a plane-parallel Fabry-Perot interferometer. This made it possible to obtain scan holograms of the process at $\lambda_1 = 0.69 \mu\text{m}$ and $\lambda_2 = 0.58 \mu\text{m}$, and to separate the contribution of electrons from that of heavy particles to the refraction of a plasma jet.

This two-wavelength holographic cinematography method was used to determine the radial distributions of the electron density and of the heavy-particle concentration at different moments in time and for different sections of laser plasma near the irradiated surface of a irradiated sample

At distances of 10 - 15 mm from the surface of a sample it was found that heavy particles ("hot" atoms and ions) of metals and molecules of atmospheric gases made only a small

contribution to refraction. At large distances (where there were no "heated" luminous particles) the contribution of the cold dense air became significant. This was due to the pushing out of air by a plasma cloud.

When either positive or negative potential is applied to the sample, many small droplets appear on its surface after the laser action (Figures 4 and 8). In particular, at the laser pulse energy 20 J, the diameter of the focusing spot 2 mm, and the electric field strength 10^6 V cm^{-1} we observed ejection of droplets having the mean characteristic size less than 0.1 mm to the distance up to 2 cm from the crater centre. The maximal characteristic size of the droplets was 0.4 mm.

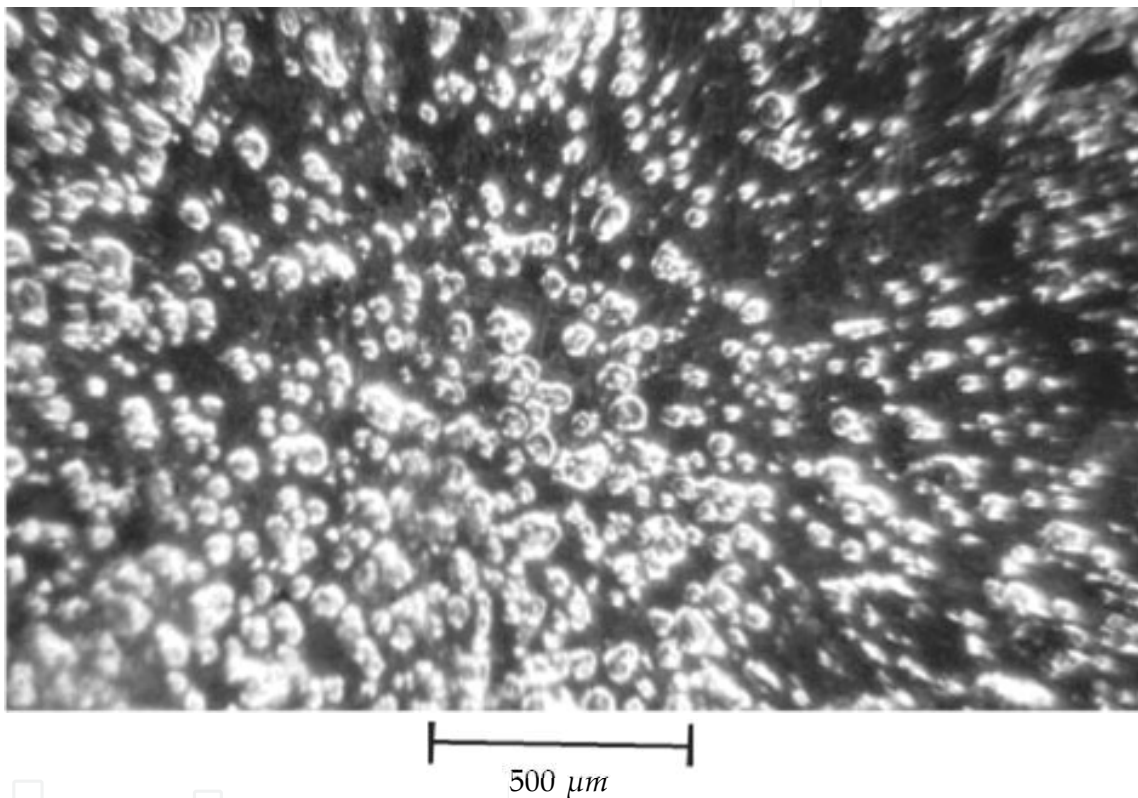


Figure 8. Microscopic surface relief of the crater outer zone photographs.

In the absence of the external electric field the mean size of the droplets was $\sim 0.4 \text{ mm}$. The droplets were seen at the distance up to $\sim 1 \text{ cm}$ from the crater centre.

In accordance with the results presented above, the dynamics of the processes on the surface of a sample, placed in an external electric field with the strength from 0 to 10^6 V m^{-1} and subject to the action of the pulsed laser radiation with the parameters mentioned above, is thought to be the following. The primary plasma formation and the initial stage of the laser torch development, in principle, do not differ from those observed in the absence of the external electric field. The metal is melted and evaporated. As a result of local formation of steam and plasma [4, 5], the erosion torch begins to form with the fine-dispersed liquid-droplets phase. Note, that the bulk evaporation is promoted by the gases, diluted in the metal, and by the spatiotemporal nonuniformity of the laser radiation [4]. At a radiation flux density $10^6 - 10^7 \text{ W}$

cm² the bulk evaporation is typical of all metals used in the experiments [5]. Obviously, the presence of the external electric field affects (increases or decreases depending on the direction of the field strength vector) the velocity of motion of the plasma front and causes some distortion of the plasma cloud shape. It is essential that the mentioned differences (at the considered parameters of laser radiation) are observed only at the initial stage of the laser plume development, because after the steam-plasma cloud reaches the electrode (3) an electric breakdown (short-circuit) occurs, and the external field in the interelectrode gap disappears.

Consider now the motion of the molten metal droplets in the steam-plasma cloud. In our opinion, the significant difference in the characteristic size of droplets, observed on the surface of the irradiated sample in the presence of the external electric field (independent of the direction of the field strength vector) and in the absence of the field, is a manifestation of the following mechanism of droplet formation [6]. It is known that at the surface of a liquid (including a liquid metal) the formation of gravity-capillary waves [7] is possible under the action of various perturbations. Undoubtedly, the examples of such perturbations are the spatially nonuniform evaporation of the target material due to nonuniform heating caused by nonuniform energy distribution over the focusing spot [8], the nonuniform primary plasma formation [6, 9, 10] caused by roughness of the irradiated sample surface [8], and, in the first place, the slop of the molten metal initiated by each spike of laser radiation, acting on the exposed sample [2].

Using the method presented in [11], one can show that at insignificant thickness of the molten metal layer (confirmed by the view of the 'outer' (directed) zone of the crater, particularly, the absence of fillets of significant height at the crater edge) the dispersion equation for the gravity-capillary waves takes the form

$$\omega^2 = \frac{\alpha k^3}{\rho} + gk - \frac{k E_0 E'}{4\pi\rho\xi'} \Big|_{z=0}, \quad (1)$$

where α is the surface tension coefficient of the molten metal; ρ is the metal density; g is the free fall acceleration; k is the magnitude of the wave vector of the gravity-capillary wave; E_0 is the electric field strength at the surface ($z = 0$) of the molten metal (the z axis is perpendicular to the surface of the irradiated sample, directed towards the laser radiation source and parallel to the vector E_0); $E' = -\partial\varphi'/\partial z$ is the perturbation of the electric field in the space surrounding the molten metal; ξ' is the small displacement of the surface of the liquid in the z axis direction in the gravity-capillary wave.

Because for the uniform field E_0 the potential is $\varphi = -E_0 \cdot z$ (the potential at the metal surface is considered to be zero), the displacement of the mentioned surface by the small quantity ξ' leads to a small distortion of the potential:

$$\varphi' \Big|_{z=0} = E_0 \cdot \xi'. \quad (2)$$

It follows from Fig. 3 that the maximal concentration of electrons in the plasma formation does not exceed $\sim .10^{18}$ cm³, which corresponds to the change in the dielectric constant of the

medium ε by approximately 10^{-5} . Therefore, near the metal surface $\varepsilon \cong 1$ and with the boundary condition (2) taken into account

$$\varphi' = E_0 \xi' e^{-kz}.$$

In this case, the dispersion equation for gravity-capillary waves takes the form

$$\omega^2 = \frac{\alpha k^3}{\rho} + gk - \frac{k^2 E_0^2}{4\pi\rho}.$$

Because the frequency of the gravity-capillary waves ω is determined by the temporal characteristics of the abovementioned perturbations and, therefore, does not depend on the strength of the electric field E_0 , the growth of the magnitude E_0 (independent of the direction of the vector \vec{E}_0) should cause the increase in the magnitude of the wave vector

$k = \frac{2\pi}{\Lambda}$ and the decrease in the wavelength Λ of the gravity-capillary wave. If we assume that the droplets are 'torn away' by the plasma flow from the 'tops' of the gravity-capillary wave and, therefore, their characteristic size is proportional to Λ , then it becomes clear why in the presence of the external electric field (of any direction) the observed mean size of the droplets becomes essentially reduced.

The escaped droplets possess the charge of the same sign as the sample. That is why the droplets begin to move with acceleration towards the second electrode. However, since the maximal initial velocity of the outgoing droplets under the analogous conditions [8] is ~ 45 m s⁻¹, i.e., an order of magnitude smaller than the velocity of steam-plasma cloud spreading, the droplets do not reach the electrode (3) before the moment of the breakdown in the interelectrode gap. In what follows (in the absence of the external electric field) the droplets move under the action of the same forces as in [8] and, therefore, in the way, described in [8]. In this case, having acquired at the stage of accelerated motion in the electric field the velocity, exceeding the initial one, the droplets may fly to a greater distance along the surface of the irradiated sample than in the absence of the electric field, which is observed in the experiment. Moreover, having moved to a greater distance from the sample surface and, therefore, being affected by the plasma for longer time before returning to the surface, the droplets may be split into finer parts than in the absence of the external field.

It should be noted that the droplets in the erosion plume may appear not only due to the molten pool surface instability, but also due to the condensation of the steams of the erosion products [12, 13]. Moreover, since the droplets produced in the course of condensation of steams may be charged [14], they, similar to those carried out from the molten pool, in the electric field may be removed from the crater to a greater distance than in the absence of the electric field. However, this mechanism of plasma formation is dominating under somewhat different conditions of laser radiation acting on the material [12 – 15], namely, at significantly greater mean radiation flux density ($\sim 10^8 - 10^9$ W cm⁻²) and smaller exposure duration (single pulses of laser radiation were used with the duration $\sim 100 - 200$ ns and

with less smooth temporary shape). In the case of such a regime of laser metal processing one observes the screening of the irradiated sample by the plasma cloud, which is possible only at the concentration of the ablated material steam essentially exceeding 10^{18} cm^{-3} (see Fig. 6). In this case, one observes intense formation of droplets with the dimension $\sim 200 \text{ nm}$ and smaller, and this process is most active at the late stages of laser radiation action on the material (at decreasing intensity of laser action) [15] and even after its termination [12]. At smaller radiation flux density, characteristic of the experiment considered in the present work ($\sim 10^{18} \text{ cm}^{-3}$), droplet condensation from the steam of ablation products is expected to be less intense. Therefore, the essential contribution of the condensation mechanism to the process of formation of large drops (having the size $\sim 0.1 - 0.4 \text{ mm}$, see Figures 4 and 8), especially at early stages of the process, i.e., before filling the entire interelectrode gap by the plasma cloud, seems to be hardly probable.

3. Acoustic waves generation

Investigating the acoustic emission let us use the model of a loaded zone radiating waves into elastic medium. Corresponding to this model let us consider the destructed zone as a spherical segment with the curvature radius R , depth d and diameter $2r_1$. z -ax of the coordinate system is directed along the laser beam. It is important that the parameters of the irreversibly deformed zone are changing on the time:

$$R = R(t), \quad d = d(t), \quad r_1 = r_1(t);$$

here t is the time.

The displacement vector in an elastic zone consists of a longitudinal and a transversal components, $\vec{A} = \vec{A}_l + \vec{A}_t$, and each of them can be described by corresponding wave equation. Because of the presence of the media board direct in the elastic wave generating zone the solution of the wave equations system we shall search as a sum of the volume and the surface components

$$\begin{aligned} \vec{A}_l &= \vec{A}_{lO} + \vec{A}_{l\Pi} = \nabla \psi_O + \nabla \psi_{\Pi}, \\ \vec{A}_t &= \vec{A}_{tO} + \vec{A}_{t\Pi} = \vec{A}_{tO} + \text{rot}(\vec{B}). \end{aligned}$$

With regard to the symmetry of our problem, $\vec{A}_{tO} = 0$, scalar potential

$$\psi_O(\omega) = -\tilde{A}(\omega) \cdot \frac{\exp(-ik_l r)}{r},$$

$$B_\rho = B_z = 0,$$

$$\psi_{\Pi}(\omega) = -Z_0(k_R \rho) \cdot (\tilde{B}(\omega) \cdot \exp(-\chi_l z) + \tilde{Q}(\omega) \cdot \exp(\chi_l z)),$$

$$B_\varphi(\omega) = Z_1(k_R \rho) \cdot (\tilde{D}(\omega) \cdot \exp(-\chi_t z) + \tilde{S}(\omega) \cdot \exp(\chi_t z)).$$

Here ω is a frequency, $k_t = \omega/c_t$, c_t and c_t – longitudinal and transversal sound velocities,

$\tilde{A}(\omega)$ – wave amplitude, $k_R = \omega/c_R$, c_R – surface wave velocity,

$\chi_i = (k_R^2 - k_i^2)^{1/2}$, $\tilde{B}(\omega)$, $\tilde{D}(\omega)$, $\tilde{Q}(\omega)$, $\tilde{S}(\omega)$, – os

cillation amplitudes, $Z_i(x)$ – spherical function.

When $\rho \rightarrow 0$ and $z \rightarrow \infty$ the result must remain finite, therefore $Z_i(x) = J_i(x)$ (Bessel function),

$\tilde{Q}(\omega) = \tilde{S}(\omega) = 0$, and

$$\begin{aligned} \bar{A}(\omega) = & A(\omega) \frac{\vec{r}}{r^3} (1 + ik_l r) \exp(-ik_l(r-R)) + B(\omega) (\bar{\rho}_0 k_R J_1(k_R \rho) + \bar{z}_0 \chi_l J_0(k_R \rho)) \times \\ & \times \exp(-\chi_l(z-h)) + D(\omega) (\bar{\rho}_0 \chi_l J_1(k_R \rho) + \bar{z}_0 k_R J_0(k_R \rho)) \exp(-\chi_l(z-h)) \end{aligned} \quad (3)$$

where $A(\omega) = \tilde{A}(\omega) \cdot \exp(-ik_l R)$, $B(\omega) = \tilde{B}(\omega) \cdot \exp(-\chi_l h)$, $D(\omega) = \tilde{D}(\omega) \cdot \exp(-\chi_l h)$.

Let us consider that on the surfaces $r = R$ and $z = h$ temporal dependence of pressure in the plasma cloud is

$$P|_{r=R} = p(t).$$

On the surface of spherical segment $R = R(t)$

$$\sigma_{rr} = -p(t), \quad \sigma_{r\theta} = \sigma_{r\phi} = 0;$$

on the surface $z = h$

$$\sigma_{zz} = q(t), \quad \sigma_{z\theta} = 0, \quad \sigma_{z\phi} = 0.$$

Here σ_{ij} are the components of the stress tensor, r , θ , φ are the coordinates of spherical system.

Out of the spherical segment $R = R(t)$ medium is elastic, and so

$$\begin{aligned} & \left[\lambda \left(\frac{\partial A_r}{\partial r} + 2 \frac{A_r}{r} + \frac{1}{r} \frac{\partial A_\theta}{\partial \theta} + \frac{A_\theta}{r} \operatorname{ctg} \theta \right) + 2\mu \frac{\partial A_r}{\partial r} \right]_{r=R(t)} = -p(t), \\ & \left(\frac{\partial A_\rho}{\partial z} + \frac{\partial A_z}{\partial \rho} \right)_{z=h(t), \rho=\rho_1(t)} = 0, \\ & \left[\lambda \left(\frac{\partial A_\rho}{\partial \rho} + \frac{A_\rho}{\rho} + \frac{\partial A_z}{\partial z} \right) + 2\mu \frac{\partial A_z}{\partial z} \right]_{z=h(t), \rho=\rho_1(t)} = -p(t). \end{aligned} \quad (4)$$

Here A_i are the components of the displacement vector \vec{A} , λ , μ are the Lamé coefficients.

Substituting A_i from the equation (3) to the system (4) we can calculate for each temporal moment $A(\omega, R, d, \rho_1)$, $B(\omega, R, d, \rho_1)$, $C(\omega, R, d, \rho_1)$, $\sigma_{zz}(\omega, R, d)$ and

$$\sigma_{zz}(t) = \int_{-\infty}^{+\infty} \sigma_{zz}(\omega, R, d) \text{Exp}[i\omega t] d\omega = \int_{-\infty}^{+\infty} \sigma_{zz}(\omega, R(t), d(t)) \text{Exp}[i\omega t] d\omega = \int_{-\infty}^{+\infty} \sigma_{zz}(\omega, t) \text{Exp}[i\omega t] d\omega.$$

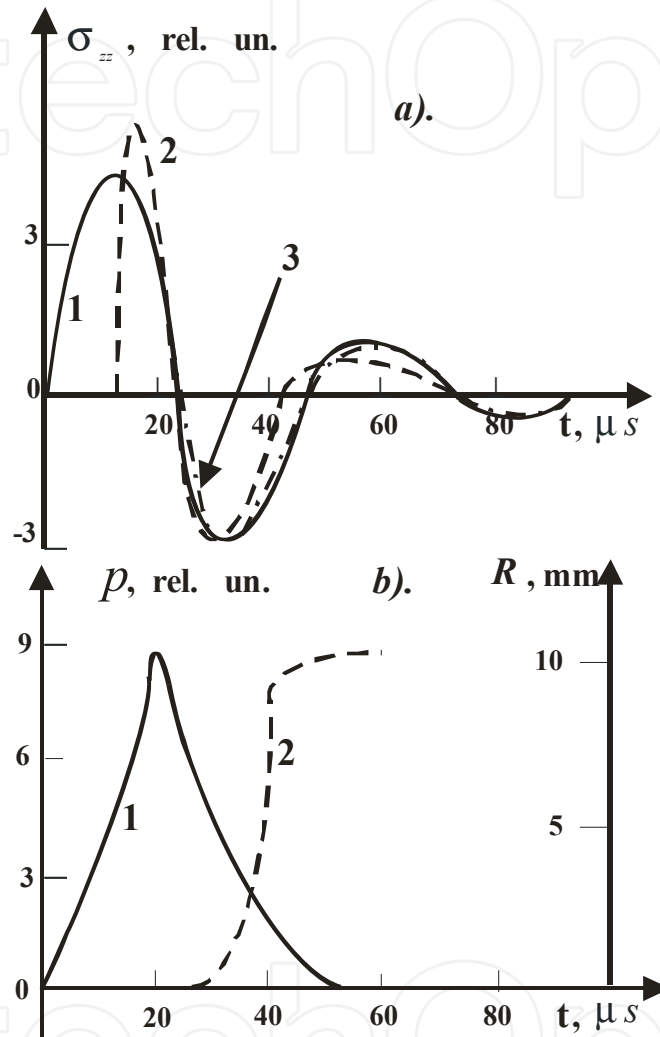


Figure 9. a). Temporal dependences of pressure of acoustic wave on the action of laser pulse with duration of 20 μs on copper sample: 1 – experimental dependence; 2 – dependence calculated without account of crater growth; 3 – dependence calculated with account of crater growth. b). 1 – temporal dependences of pressure of plasma cloud on the border of irreversibly deformed zone; 2 – temporal dependences of curvature radius.

The results of the calculations with $R(t) = R_{\max} \cdot \exp(-\frac{t^2}{\tau_0^2})$ for $t < 0$ and $R(t) = R_{\max}$ for $t > 0$ are presented on the figure 9; $\tau_0 = 40 \mu s$.

Evidently that at action on a surface of the copper sample of a rhodamine laser impulse duration $\sim 20 \mu s$ time of growth of a zone of destruction makes approximately 40 μs , that

will well be coordinated with time of existence of plasma formation at a surface of the target exposed to laser-plasma processing ($\sim 50 \mu\text{s}$). Use of model of the loaded area with the moving borders radiating acoustic waves in the elastic medium allows us to solve the important practical problem – the definition of a law of time growth of a zone of irreversible deformations on a surface of the sample exposed to pulse laser-plasma processing.

4. Laser treating of transparent insulators

Now let us to investigate the dynamics of crater growth and of changes in the density of an inelastically deformed material on the surface of a transparent insulator when it interacts with a millisecond light pulse that has a complex temporal profile. The experimental setup used in the study was similar to presented in Fig. 1. Radiation was provided by a GOR-100M ruby laser operating in the free-running regime. This made it possible to generate pulses of $\tau \sim 1.2 \text{ ms}$ duration with an energy E that could be varied within the limits 5-50 J. The radiation passed through focusing system and was directed to sample. Both single-lens and double-lens focusing systems were used; they formed an image of stop on the surface of the sample. The diameter D of the focusing spot obtained in this way was varied in the course of our experiments from 1 to 2 mm.

Part of the laser radiation was directed by the front face of the glass wedge to an IMO-2N energy meter whose entry pupil was located in the focal plane of lens. The radiation reflected by the rear face of the wedge was directed to FEK-14 coaxial photocell and the photocell signal was applied to the input of an S8-13 oscilloscope, which recorded the temporal profile of the laser pulse.

The sample was placed in a window in one of the arms of a Mach-Zehnder holographic interferometer which was illuminated by radiation from a second ruby laser operating in the free-running regime. The longitudinal modes emitted by this probe laser were selected by a Fabry -Perot etalon, used as the exit mirror, and the transverse modes were selected by a stop placed inside a resonator. The probe radiation was directed to collimator which produced a parallel beam with a diameter of $\sim 3 \text{ cm}$. A field of view of this kind was sufficient to study the growth of a crater, the changes in the density of the sample in the inelastically deformed zone, the formation and propagation of elastic waves in the sample, and the processes that occurred in the gas and in the plasma cloud near the sample.

The interferometer was in contact with an SFR-1M high-speed camera. The plane of a photographic film in the camera was made to coincide, with the aid of objective, with the conjugate plane of a meridional cross section of the light beam acting on the sample. The camera was operated in the cine mode.

Fig. 10 shows the holographic interferograms at different moments from the beginning of the interaction of a laser pulse of energy $E \approx 35 \text{ J}$ with a sample made of polymethylmethacrylate (PMMA) on which the pulse formed a focusing spot $D \approx 1 \text{ mm}$ in diameter. The temporal profile of this pulse had the form shown in Fig. 11. We used these interferograms and solved the Abel equation to find the fields representing the distributions of the refractive index $n(z, r, t)$ in space and time, and we then applied the Lorentz - Lorenz expression

$$\rho = \frac{(n^2 - 1)}{(n^2 + 2)} \frac{\mu}{R_m}$$

to find the density fields $\rho(z, r, t)$ shown in Fig. 12. Here, μ is the molar mass of the material of the sample; $R_m = 4/3\pi N$, N is the number of particles responsible for refraction in a unit volume. The ratio μ/ρ was found from the parameters of the unperturbed medium.

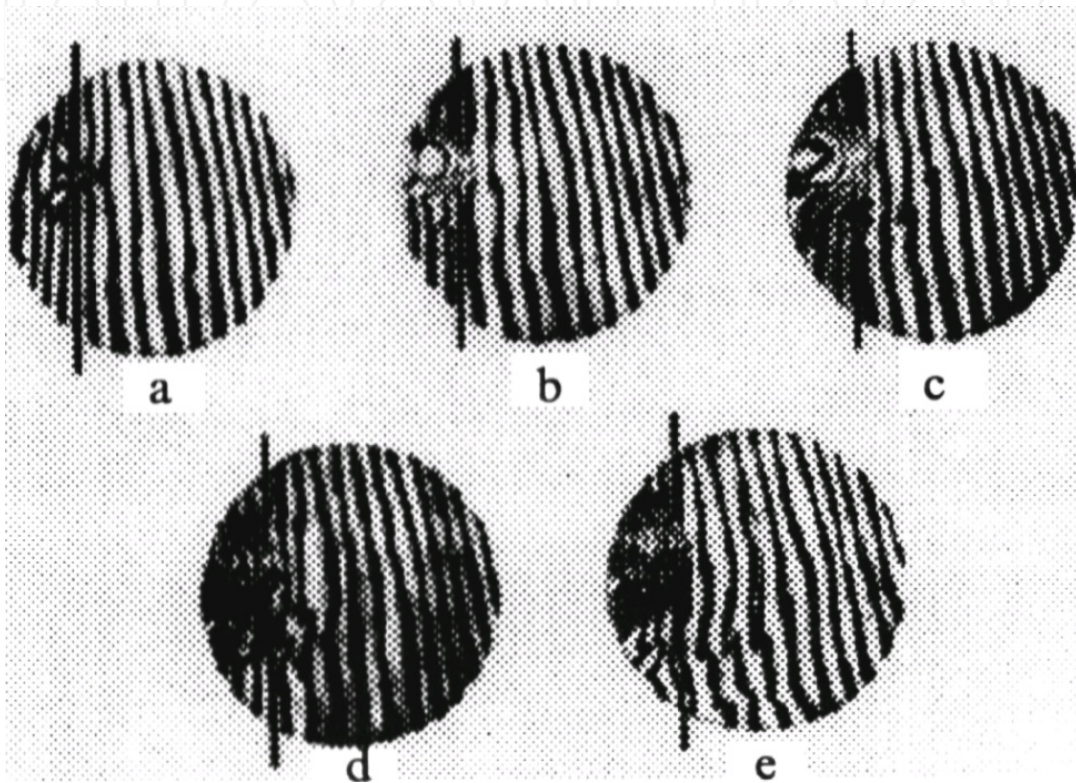


Figure 10. Interferograms recorded at the moments $t = 9.6 \mu\text{s}$ (a), $16.0 \mu\text{s}$ (b), $25.6 \mu\text{s}$ (c), $48.0 \mu\text{s}$ (d), and $70.4 \mu\text{s}$ (e) relative to the beginning of the interaction.

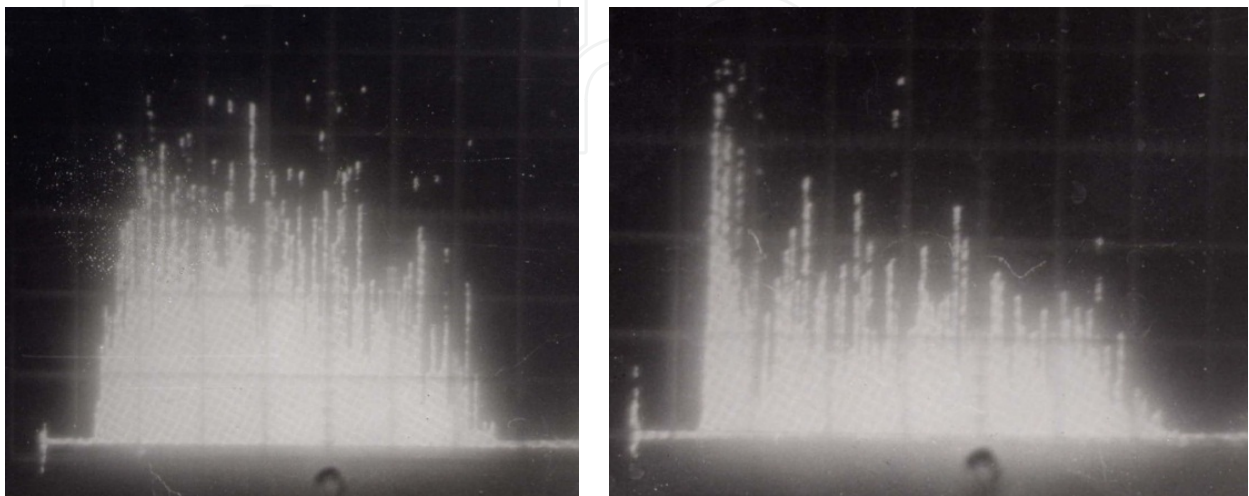


Figure 11. Temporal profile of a laser pulse before and after passing of a sample

Fig. 12 also shows the profiles of a crater formed on the surface of PMMA and recorded at different moments. These profiles yielded the time dependences of the diameter d , depth h , and volume V of the crater (Fig. 13). Fig. 14 shows the dependences of the final diameter, depth and volume of the crater on the energy of the light pulse interacting with the surface of PMMA.

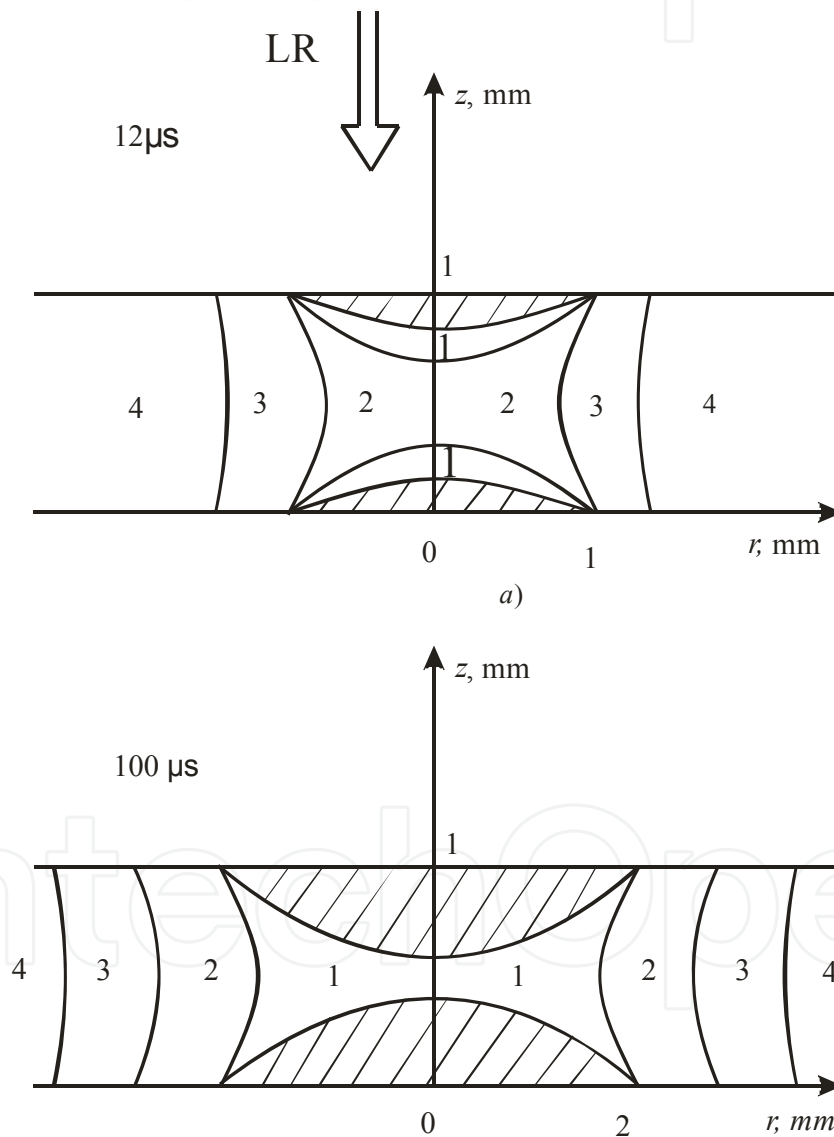


Figure 12. Profile of a crater and of a constant-density field at the moments $t = 12 \mu\text{s}$ (a) and $100 \mu\text{s}$ relative to the beginning of the interaction.

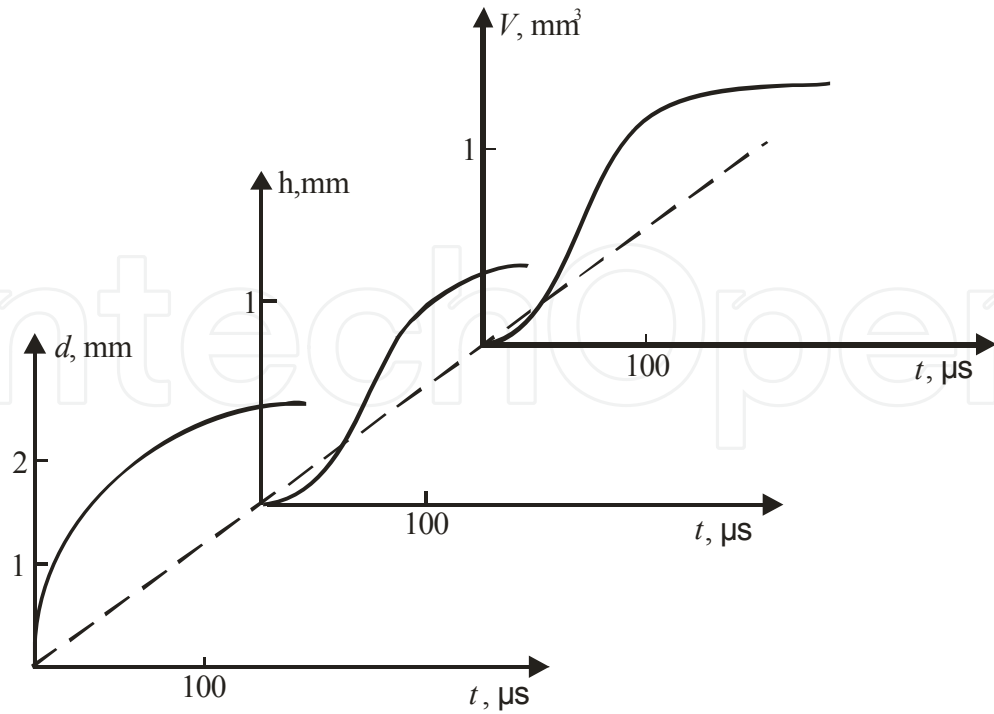


Figure 13. Crater diameter, depth, and volume time dependences.

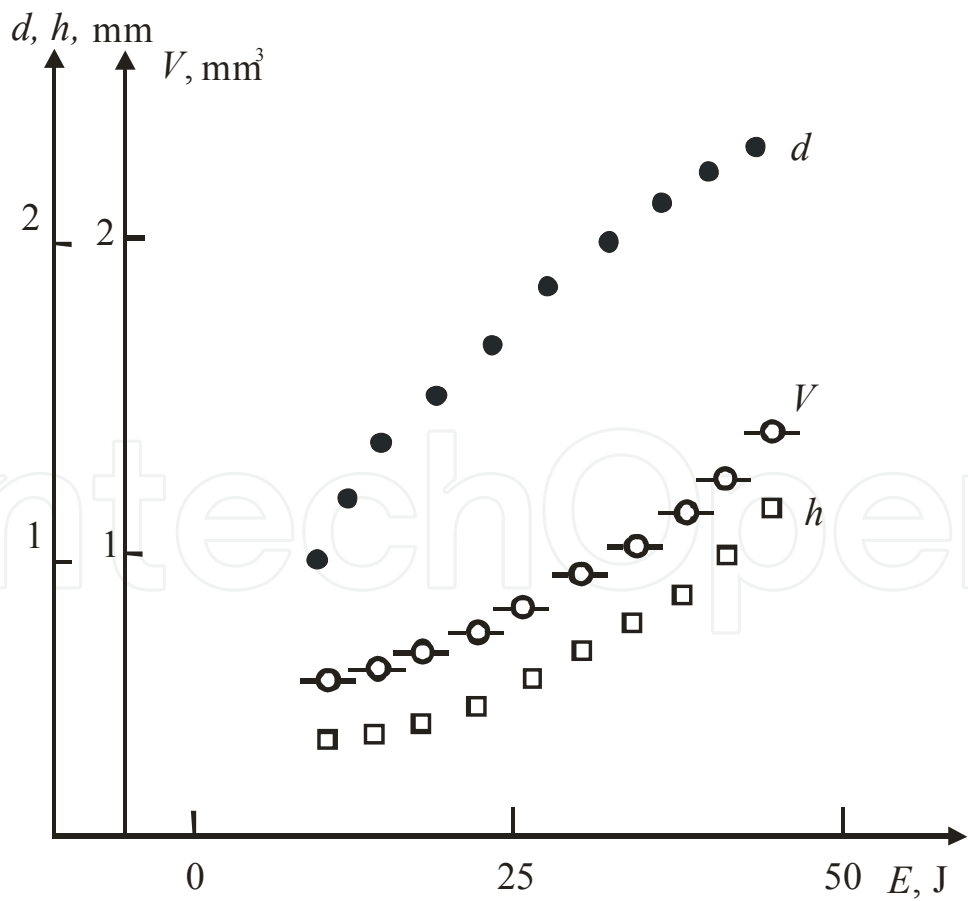


Figure 14. Dependences of the final diameter, depth and volume of a crater on the energy of a laser pulse.

5. Discussion of results

First of all, it is worth noting that the time dependences of the diameter d , depth h , and volume V of the crater (Fig. 13) were smooth and did not react in any way to the separate spikes of the laser pulse profile $E(f)$. The dependences $d(t)$, $h(t)$, and $V(t)$ were found to be similar for the same value of

$$E(t) = 2\pi \int_0^t \int_0^{r_0} q(\tau) d\tau dr$$

irrespective of the profile $q(t)$ (which varied in a random manner from one pulse to the next). The constant-density surfaces changed equally smoothly (Fig. 4).

Obviously, even in the case of a very high power density ($\sim 10 \text{ MW cm}^{-2}$) the energy of a single spike ($\sim 0.1 \text{ J}$) was insufficient to stimulate any significant ejection of the mass of the target.

The growth of the crater and the temperature rise in the region adjoining the target surface (it was the temperature rise that altered the density of the target material) were in this case determined by the normal evaporation process, in spite of the appearance of a laser-plasma jet (Fig. 10; the presence of a plasma was detected in an analysis of the field $n(z, r)$ by a method similar to that described in [3]). This was deduced from the observation that the mass of the evaporated material $m(I)$ was governed entirely by the energy E_t (more exactly, by the absorbed energy which was related to E_t).

It is also worth noting the observation (Fig. 14) that an increase in the energy E of a laser pulse first resulted in an increase in the final size of the crater because of the preferential increase in its diameter d . When d reached $\sim 1.5D$, the three-dimensional crater growth began. In the first stage the volume V varied in accordance with the law (Fig. 14)

$$V = D \exp[C(E - E_0)] \quad (5)$$

where $E \approx 7 \text{ J}$, $C \approx 0.2 \text{ J}^{-1}$, and $D = 0.05 \text{ mm}^3$, whereas in the second stage it obeyed the law

$$V = V_b + A(E - E_0)^\alpha, \quad (6)$$

where $\alpha \approx 1.5$, $A \approx 2 \text{ mm}^3 \text{ J}^{-3/2}$, and $V_b \sim 0.5 \text{ mm}^3$ (governed by the volume V at which the change in the volume became different).

It is important to note that when the energy E was sufficient for the observation of both stages, the crater varied with time in exactly the same manner as before: first its diameter d increased and the three-dimensional growth was observed only from $d \sim 1.5 D$.

The nature of the crater growth was, in our opinion, governed by the temperature distribution $T(z, r)$ in the sample being irradiated (we recall that $T(z, r)$ governs the density distribution $\rho(z, r)$; see Fig. 12). In fact, along the crater perimeter the density and

temperature gradients can exceed considerably $|\text{grad } \rho|$ and $|\text{grad } T|$ on the axis of the system (the z axis), which is to be expected because a transparent sample is exposed to a light beam with sharp boundaries. This sharpness of the boundaries is responsible for a high value of $|\text{grad } T|$ at the perimeter of the focusing spot. On the other hand, the transparency of the medium results in a practically homogeneous (and weak) absorption of the energy in layers with different values of z and it is responsible for the low value of $|\text{grad } T|$ in this direction.

Since the thermal energy flux is $q \sim -\text{grad}(T)$, the peripheral (relative to the axis of the system) part of the sample surface is heated strongly. For this reason the evaporation is strong in the same region. Since the mass of the evaporated material is

$$\Delta m = \rho h \Delta S = \Delta g_t / \beta \sim \Delta E S / L_b,$$

where β is the heat of evaporation, we find that

$$S \sim \exp E / (\rho h L_b),$$

in good agreement with equation (5) when h is almost constant (because the component of $\text{grad } T$ directed along the z axis is small).

When the boundaries of the evaporation zone spread beyond the focusing spot, the temperature gradient at the perimeter of this spot decreases, resulting finally in the equalization of the gradient over the whole crater profile. The heat flux also becomes equalized in all directions and the evaporation process is then three-dimensional. We are now in the second stage of the process when $\Delta d \sim \Delta h$.

If we assume that the crater is a spherical segment (in the case of a shallow crater we have $h \ll d$ and since the crater were shallow in our experiments, this is justified as a first approximation), then

$$\Delta V = 4\pi R^2 \Delta R,$$

where R is the radius of curvature of the crater.

In the case of the processes exhibiting axial symmetry (which was true of the process we investigated) we have $R \sim E^{1/2}$ [16] and therefore $V \sim E^{3/2}$, which is in good agreement with equation (6).

The crater growth practically stopped after $t_{max} \sim 100 \mu s$ from the beginning of the interaction with the target (we recall that the pulse duration was $\tau \approx 1.2$ ms) and t_{max} depended weakly on E . Obviously, at the power densities of the light flux used in our investigation the energy absorbed at $t > t_{max}$ was no longer sufficient to maintain the vaporization temperature on the surface of the grown crater. The plasma cloud was still maintained near the target surface and, consequently, local (and resulting in a much smaller loss of mass) vaporization still continued.

6. Conclusions

The studies performed have shown that under the action of laser radiation with the mean radiation flux density $\sim 10^6 - 10^7 \text{ W/cm}^2$ the surface of metals in the external electric field with different polarity and the strength up to 10^6 V m^{-1} the characteristic size of the target substance droplets, carried out of the irradiated zone, decreases by several times with increasing external electric field strength. Probably, this is due to a change in the wavelength of the gravity-capillary wave, excited on the molten metal surface. The observed effect offers the possibility to control the size of the metallic droplets in the course of laser deposition of thin films.

At action on a surface of the copper sample of a rhodamine laser impulse duration $\sim 20 \mu\text{s}$ time of growth of a zone of destruction makes approximately 40 мкс , that will well be coordinated with time of existence of plasma formation at a surface of the target exposed to laser-plasma processing ($\sim 50 \mu\text{s}$). Use of model of the loaded area with the moving borders radiating acoustic waves in the elastic medium allows to solve the important practical problem – the definition of a law of time growth of a zone of irreversible deformations on a surface of the sample exposed to pulse laser-plasma processing.

The effective growth of a crater formed as a result of the interaction of a laser pulse of duration of at least $\sim 1 \text{ ms}$ with the surface of a transparent insulator did not last more than $100 \mu\text{s}$. Initially, the area of the crater increased and then, but only after it was twice as large as the focusing spot, the damage region began to grow in three dimensions. The crater growth dynamics was governed primarily by the evaporation mechanism: the individual spikes of a laser pulse interacting with the target did not influence the growth process.

Author details

A. Yu. Ivanov and S. V. Vasiliev
Grodno State University, Grodno, Belarus

7. References

- [1] Ivanov A.Yu. Acoustic diagnostics of materials laser treating process. Grodno: GrSU, 2007.
- [2] Bosak NA., Vasil'ev S.V., Ivanov A.Yu., Min'ko L.Ya., Nedolugov VI., Chumakov A.N. *Kvantovaya Elektron.*, 27, 69 (1999) [*Quantum Electron.*, 29, 69 (1999)].
- [3] Barikhin B.A., Ivanov A.Yu., Nedolugov VI. *Kvantovaya Elektron.*, 17, 1477 (1990) [*Sov. J. Quantum Electron.*, 20, 1386 (1990)].
- [4] Goncharov V.K., Kontsovoy V.L., Puzyrev MV. *Inzhenerno IZicheskiy zhurnal*, 66, 662 (1994) [*Journal of Engineering Physics and Thermophysics*, 66, 588 (1994)].
- [5] Goncharov V.K., Kontsevoy V.L., Puzyrev MV. *Kvantovaya Elektron.*, 22, 249 (1995) [*Quantum Electron.*, 25, 232 (1995)].

- [6] Zaykin A.E., Levin A.V., Petrov AL., Stranin S.A. *Kvantovaya Elektron.*, 18, 708 (1991) [*Sov. J. Quantum Electron.*, 21, 643 (1991)].
- [7] Zaykin A.E., Levin A.V., Petrov AL. *Kvantovaya Elektron.*, 21, 486 (1994) [*Quantum Electron.*, 24, 449 (1994)].
- [8] Vasil'ev S.V., Ivanov A.Yu., Lyalikov AM. *Kvantovaya Elektron.*, 22, 830 (1995) [*Quantum Electron.*, 25, 799 (1995)].
- [9] Dorofeev IA., Libenson MN. *Opt. Spektrosk.*, 76,73(1994) [*Opt. Spectrosc.*, 76, 66 (1994)].
- [10] Chumakov AN. et al. *Kvantovaya Elektron.*, 21, 773 (1994) [*Quantum Electron.*, 24, 718 (1994)].
- [11] Rabinovich MI., Trubetskov DI. *Vvedenie v teoriyu kolebanii i voln* (Introduction to the Theory of Oscillations and Waves) (Moscow: Nauka, 1984).
- [12] Goncharov V.K., Kozadayev K.V. *Inzhenerno-fizicheskii zhurnal*, 83, 80 (2010) [*Journal of Engineering Physics and Thermophysics*, 83, 90 (2010)].
- [13] Chumakov AN., Bereza NA., Hu Dz.D., Bosak NA., Guo Z.H., Hie K.K. *Inzhenerno-fizicheskiizhurnal*, 84, 524 (2011)[*Journal of Engineering Physics and Thermophysics*, 84, 567 (2011)].
- [14] Klimentov SM. et al. *Laser Phys.*, 8 (6), 1(2008).
- [15] Goncharov V.K., Kozadayev K.V., Shchegrikovich DV. *Inzhenerno-flzicheskiizhurnal*, 84, 781 (2011) [*Journal of Engineering Physics and Thermophysics*, 84, (2011)].
- [16] Ashmarin I.I, Bykovskii Yu A, Gridin V A, et al. *KvantovayaElektron. (Moscow)* 6 1730 (1979) [*Sov. J. Quantum Electron.* 9 1019(1990)].